

**Accelerated Article Preview****Low-loss contacts on textured substrates for inverted perovskite solar cells**

---

Received: 28 June 2023

---

Accepted: 12 October 2023

---

Accelerated Article Preview

---

Published online: 23 October 2023

---

Cite this article as: Park, S. M. et al.

Low-loss contacts on textured substrates for inverted perovskite solar cells. *Nature* <https://doi.org/10.1038/s41586-023-06745-7> (2023)

---

**So Min Park, Mingyang Wei, Nikolaos Lempesis, Wenjin Yu, Tareq Hossain, Lorenzo Agosta, Virginia Carnevali, Harindi R. Atapattu, Peter Serles, Felix T. Eickemeyer, Heejong Shin, Maral Vafaie, Deokjae Choi, Kasra Darabi, Eui Dae Jung, Yi Yang, Da Bin Kim, Shaik M. Zakeeruddin, Bin Chen, Aram Amassian, Tobin Filleter, Mercuri G. Kanatzidis, Kenneth R. Graham, Lixin Xiao, Ursula Rothlisberger, Michael Grätzel & Edward H. Sargent**

---

This is a PDF file of a peer-reviewed paper that has been accepted for publication. Although unedited, the content has been subjected to preliminary formatting. Nature is providing this early version of the typeset paper as a service to our authors and readers. The text and figures will undergo copyediting and a proof review before the paper is published in its final form. Please note that during the production process errors may be discovered which could affect the content, and all legal disclaimers apply.

# 1 **Low-loss contacts on textured substrates for inverted perovskite solar cells**

2 So Min Park<sup>1,2,10</sup>, Mingyang Wei<sup>3,10</sup>, Nikolaos Lempesis<sup>4,10</sup>, Wenjin Yu<sup>5</sup>, Tareq Hossain<sup>6</sup>, Lorenzo  
3 Agosta<sup>4</sup>, Virginia Carnevali<sup>4</sup>, Harindi R. Atapattu<sup>6</sup>, Peter Serles<sup>7</sup>, Felix T. Eickemeyer<sup>3</sup>, Heejong  
4 Shin<sup>1</sup>, Maral Vafaie<sup>2</sup>, Deokjae Choi<sup>1</sup>, Kasra Darabi<sup>8</sup>, Eui Dae Jung<sup>2</sup>, Yi Yang<sup>1</sup>, Da Bin Kim<sup>2</sup>, Shaik  
5 M. Zakeeruddin<sup>3</sup>, Bin Chen<sup>1</sup>, Aram Amassian<sup>8</sup>, Tobin Filleter<sup>7</sup>, Mercouri G. Kanatzidis<sup>1</sup>, Kenneth  
6 R. Graham<sup>6</sup>, Lixin Xiao<sup>5</sup>, Ursula Rothlisberger<sup>4</sup>, Michael Grätzel<sup>3†</sup> & Edward H. Sargent<sup>1,2,9†</sup>

7 <sup>1</sup>Department of Chemistry, Northwestern University, Evanston, Illinois 60208, United States.

8 <sup>2</sup>Department of Electrical and Computer Engineering, University of Toronto, Toronto, Ontario,  
9 M5S 3G4, Canada.

10 <sup>3</sup>Laboratory of Photonics and Interfaces, Ecole Polytechnique Fédérale de Lausanne, Lausanne,  
11 1015, Switzerland.

12 <sup>4</sup>Laboratory of Computational Chemistry and Biochemistry, Ecole Polytechnique Fédérale de  
13 Lausanne, Lausanne, 1015, Switzerland.

14 <sup>5</sup>State Key Laboratory for Artificial Microstructure and Mesoscopic Physics, Department of  
15 Physics, Peking University, Beijing 100871, P. R. China.

16 <sup>6</sup>Department of Chemistry, University of Kentucky, Lexington, KY, 40506, United States.

17 <sup>7</sup>Department of Mechanical and Industrial Engineering, University of Toronto, Toronto, Ontario,  
18 M5S 3G8, Canada.

19 <sup>8</sup>Department of Materials Science and Engineering, and Organic and Carbon Electronics  
20 Laboratories (ORaCEL), North Carolina State University, Raleigh, NC, 27695, United States.

21 <sup>9</sup>Department of Electrical and Computer Engineering, Northwestern University, Evanston, Illinois  
22 60208, United States.

23 <sup>10</sup>These authors contributed equally to this work: So Min Park, Mingyang Wei, Nikolaos Lempesis

24 †e-mail: [ted.sargent@northwestern.edu](mailto:ted.sargent@northwestern.edu); [michael.gratzel@epfl.ch](mailto:michael.gratzel@epfl.ch)

25



26 Inverted perovskite solar cells (PSCs) promise enhanced operating stability compared to  
27 their normal-structure counterparts<sup>1-3</sup>. To improve efficiency further, it is crucial to  
28 combine effective light management with low interfacial losses<sup>4,5</sup>. Here we develop a  
29 conformal self-assembled monolayer (SAM) as the hole-selective contact on light-managing  
30 textured substrates. Molecular dynamics simulations indicate cluster formation during  
31 phosphonic acid adsorption leads to incomplete SAM coverage. We devise a co-adsorbent  
32 strategy that disassembles high-order clusters, thus homogenizing the distribution of  
33 phosphonic acid molecules, thereby minimizing interfacial recombination and improving  
34 electronic structures. We report a lab-measured power-conversion efficiency (PCE) of 25.3%  
35 and a certified quasi-steady-state PCE of 24.8% for inverted PSCs, with a photocurrent  
36 approaching 95% of the Shockley-Queisser maximum. An encapsulated device having a PCE  
37 of 24.6% at room temperature retains 95% of its peak performance when stressed at 65°C  
38 and 50% relative humidity following >1000 hours of maximum power point tracking under  
39 1-sun illumination. This represents one of the most stable PSCs subjected to accelerated  
40 ageing – achieved with a PCE surpassing 24%. The engineering of phosphonic acid  
41 adsorption on textured substrates offers a promising avenue for efficient and stable PSCs. It  
42 is also anticipated to benefit other optoelectronic devices that require light management.

43 Perovskite solar cells (PSCs) have recently attained a certified efficiency of 26.1%<sup>6</sup>; however, the  
44 very highest PCE devices have yet to meet operating stability under accelerated ageing tests<sup>5</sup>. The  
45 limited device stability is attributed to the presence of mobile and hygroscopic p-type dopants in  
46 hole-transporting layers, which undermine moisture and thermal stability<sup>7</sup>. Inverted PSCs present  
47 a solution by utilizing undoped hole-selective contacts<sup>8</sup>. Recent studies have shown PCEs  
48 surpassing 25% for inverted PSCs<sup>2</sup>. However, when adhering to the stringent quasi-steady-state  
49 (QSS) protocol, their certified efficiency (~24%) requires further improvement<sup>3,9</sup>.

50 Efforts to improve inverted PSC efficiency have focused on interface passivation<sup>2,9,10</sup>. This  
51 approach suppresses non-radiative recombination and thus improves fill factors and  
52 photovoltages<sup>11</sup>. Nevertheless, higher photocurrents are needed for efficiency gains. In normal-  
53 structure PSCs, this has been realized using textured fluorine-doped tin oxides (FTO) as the  
54 transparent conductive oxides (TCO)<sup>4,5</sup>. The pyramidal grains on FTO minimize reflection losses  
55 and extend the length of the average optical path<sup>4</sup>. By contrast, inverted PSCs, often built on  
56 smooth indium tin oxides (ITO)<sup>9,10</sup>, face substantial optical losses due to the lack of light  
57 management.

58 The discrepancy is ascribed to differences in transporting materials and deposition techniques. In  
59 normal-structure PSCs, inorganic hole-blocking layers are conformally deposited on textured  
60 substrates using spray pyrolysis and chemical bath deposition<sup>4,5</sup>. However, inverted PSCs typically  
61 employ ultra-thin (<5 nm) organic hole-selective contacts on substrates<sup>2,3</sup>, which can be  
62 challenging to deposit uniformly using solution processing<sup>12</sup>. Inhomogeneity leads to energy losses  
63 and insufficient carrier extraction<sup>13</sup>.

64 Self-assembled monolayers (SAMs), particularly those composed of phosphonic acid molecules  
65 with hole-selective tail groups, have shown promise in addressing this issue<sup>14</sup>. Phosphonic acids  
66 establish coordinative/covalent bonds with TCOs, allowing for sufficient SAM coverage on rough  
67 surfaces<sup>15</sup>. This could provide a low-loss interface, uniting light management with interface  
68 passivation. Indeed, photocurrent improvements have been observed when replacing SAM-  
69 modified ITO with FTO substrates in inverted PSCs<sup>16</sup>.

70 Despite the promise, achieving a high-density, closely packed SAM remains challenging, which  
71 leads to erratic interfacial properties<sup>17</sup>. For example, M. Liu et al. revealed that phosphonic acids  
72 failed to fully cover textured wafers, which affected the performance of tandem solar cells<sup>18</sup>. Even

73 on flat substrates, the formation of SAMs tends to be non-uniform, a problem usually attributed to  
74 the limited solubility of phosphonic acids<sup>19</sup> and their insufficient chemical bond formation with  
75 metal oxides<sup>20</sup>.

76 Several strategies have been proposed to ensure conformal SAM coverage, such as utilizing more  
77 reactive oxide surfaces (e.g., nickel oxides) to promote hetero condensation<sup>18</sup>, employing thermal  
78 evaporation for SAM deposition<sup>21</sup>, and designing highly soluble phosphonic acid molecules<sup>19</sup>.  
79 However, these methods can be laborious, requiring time-intensive molecule design, synthesis,  
80 and vacuum-based layer deposition. Additionally, the use of highly reactive oxides could  
81 compromise device stability due to redox reactions with ammonium halides<sup>22</sup>.

## 82 **Molecular dynamics simulations**

83 We sought to deepen understanding of how phosphonic acids interact with textured TCOs. We  
84 began by looking at the case of 2-(9H-carbazol-9-yl)ethylphosphonic acid (2PACz), an organic  
85 molecule (Fig. 1a) capable of forming SAMs on TCOs<sup>14</sup>, and investigated its interactions with  
86 FTO. 2PACz has found extensive applications as a hole-selective contact in PSCs in view of its  
87 excellent defect passivation and deep highest occupied molecular orbital (HOMO) level<sup>21</sup>. The  
88 surface properties of FTO were approximated using tin oxides (SnO<sub>2</sub>), given that commercial FTO  
89 has a fluorine-doping level under 0.5% (atomic percentage)<sup>23</sup>. Flat vs. corrugated SnO<sub>2</sub> were  
90 analysed to understand the effects of surface morphology (Supplementary Fig. 1).

91 Molecular dynamics (MD) simulations suggest that 2PACz molecules can agglomerate, forming  
92 dimers, trimers, and tetramers (Fig. 1b and Supplementary Fig. 2). Within the initial 1 nanoseconds  
93 of simulations, 90% of the final number of clusters has been reached (Fig. 1b), and dimers were  
94 the most prevalent among clusters (Fig. 1c). Compared to flat surfaces, textured surfaces led to  
95 more clusters (e.g., 7 vs. 0 for 20 2PACz molecules on 6-nm-wide SnO<sub>2</sub>) (Supplementary Note 1;  
96 Supplementary Figs. 3 and 4). The cluster formation is closely linked to the inhomogeneity of  
97 SAMs on FTO. For instance, when 162 2PACz molecules are positioned on top of textured SnO<sub>2</sub>  
98 surfaces, despite their initial random distribution (Supplementary Video 1), the final equilibrated  
99 structures exhibit clear phase segregation (Fig. 1d), where almost 85% of the SnO<sub>2</sub> surface remains  
100 uncovered by any 2PACz molecules (Supplementary Fig. 5). These observations were also verified  
101 in a larger system (22-nm width; 1134 2PACz molecules) (Supplementary Fig. 6).

102 Reasoning that a thiol group ( $-SH$ ) could interact with phosphonic acids, and a carboxyl group  
103 ( $-COOH$ ) attached to FTO, we introduced 3-mercaptopropionic acid (3-MPA) (Fig. 1a) in  
104 simulations to break apart 2PACz clusters particularly on textured substrates. The approach is akin  
105 to the co-adsorbent strategy used in dye-sensitized solar cells to reduce dye aggregation on  
106 titanium oxides<sup>24</sup>. Similar strategies have been employed to improve the quality of hole-selective  
107 SAMs<sup>25,26</sup>. With 3-MPA at a molar ratio of 1:9 with 2PACz, we saw a relative 15% decrease in  
108 the number of clusters on textured surfaces (Fig. 1b), and a slower formation rate ( $20\text{ ns}^{-1}$  vs.  $28$   
109  $\text{ns}^{-1}$ ) (Supplementary Fig. 7). In particular, the higher-order clusters (trimers and tetramers)  
110 decreased by 53% (Fig. 1c). As a result, the mixed system shows less phase segregation (Fig. 1e  
111 and Supplementary Video 2), leading to extended surface coverage (67% vs. 15%) by 2PACz  
112 molecules (Supplementary Fig. 5). Ab initio MD (AIMD) simulations (Supplementary Note 2 and  
113 Supplementary Fig. 8) indicate that the presence of 3-MPA hinders the free movement of  
114 individual 2PACz molecules by forming a supramolecular structure (Fig. 1f). This reduces  
115 agglomeration with already-formed dimers, suppressing the formation of higher-order clusters  
116 (Supplementary Video 3). Density functional theory (DFT) calculations revealed surface binding  
117 energies of  $-3.2\text{ eV}$  and  $-2.6\text{ eV}$  for 2PACz and 3-MPA, respectively, which are much stronger  
118 than the interaction energies of 2PACz clusters ( $-0.3$  to  $-0.1\text{ eV}$  per molecule). This indicates  
119 robust anchoring of 2PACz and 3-MPA molecules upon contact with substrate surfaces.

## 120 **Characterization of organic contacts**

121 We deposited both 2PACz and a mixture of 2PACz:3-MPA on FTO substrates using solution  
122 processing, followed by annealing the film at  $100^\circ\text{C}$  and solvent washing (Methods). Micelles  
123 were detected in the processing solutions through dynamic light scattering (DLS) (Supplementary  
124 Fig. 9). However, due to their limited proportion in the volume distribution compared to 2PACz  
125 monomers, film formation primarily resulted from molecular diffusion rather than direct micellar  
126 adsorption<sup>27</sup>.

127 The film composition and its interaction with FTO substrates were investigated using X-ray  
128 photoelectron spectroscopy (XPS) and attenuated total reflectance Fourier transform infrared  
129 spectroscopy (ATR-FTIR), respectively. For the film comprising solely 2PACz molecules (the  
130 control), the presence of 2PACz was evidenced by the appearance of the phosphine (P) doublet  
131 peak (Fig. 2a) and the characteristic C-N peak and C-C/C-H peak (Supplementary Fig. 10) in the

132 XPS spectra<sup>21</sup>. In the case of mixed film, 3-MPA was indicated by the sulfur (S) 2*p* doublet peak  
133 at around 163.8 eV (i.e., the thiol group) (Fig. 2a)<sup>28</sup>. From ATR-FTIR, bidentate or tridentate  
134 binding was identified as the mode of 2PACz-FTO interactions, given the appearance of the  
135 symmetric PO<sub>3</sub><sup>2-</sup> stretching (at 996 cm<sup>-1</sup> for the control sample)<sup>29,30</sup> and the disappearance of P–  
136 OH vibrations<sup>14</sup>. These also indicated that solvent washing removed unbound molecules<sup>14</sup>. With  
137 3-MPA addition, a redshift of approximately 5 cm<sup>-1</sup> was observed for the PO<sub>3</sub><sup>2-</sup> vibrational mode,  
138 indicating the enhanced surface binding of 2PACz – as confirmed by AIMD simulations  
139 (Supplementary Note 3; Supplementary Figs. 11 and 12). ATR-FTIR of the FTO/3-MPA sample  
140 (Fig. 2b) further showed carboxylate-related peaks and a reduction in the intensity of the C=O  
141 peak, which correspond to the bidentate chelation of 3-MPA with FTO surfaces<sup>31</sup>. Combining the  
142 results from XPS and ATR-FTIR, we reasoned that 3-MPA functioned as a co-adsorbent,  
143 modulating the interaction of 2PACz with FTO substrates.

144 The resultant SAM uniformity was characterized by Kelvin probe force microscopy (KPFM).  
145 Topography images revealed that, despite varying SAM modifications, the surface morphology of  
146 FTO substrates was retained due to the ultra-thin nature of SAMs (Supplementary Fig. 13). From  
147 the respective contact potential difference (CPD) maps (Fig. 2c), we recorded surface potential  
148 variations on 2PACz-modified surfaces within a range of 120 mV. A Gaussian fit of the single  
149 peak in the CPD distribution yielded the full-width half-maximum (FWHM) of 37 mV  
150 (Supplementary Fig. 14). Introducing 3-MPA enhanced the homogeneity of electronic properties  
151 on SAM-modified surfaces, as reflected by a narrower CPD distribution with the FWHM of 22  
152 mV.

153 To directly visualize the distribution of SAMs on FTO substrates, we performed high-angle  
154 annular dark-field (HAADF) scanning transmission electron microscopy (STEM) measurements.  
155 Fig. 2d shows cross-sectional HAADF-STEM images of both control and mixed samples. Because  
156 of the contrast in the atomic number<sup>2</sup>, SAM was discernible as a dark layer sandwiched between  
157 the brighter FTO and protective molybdenum oxide (MoO<sub>x</sub>) layers. For the control SAM, we  
158 observed thickness variations across the same FTO facet, with certain regions showing thicknesses  
159 less than 1 nm. This suggests a low-density coverage and inhomogeneous distribution of 2PACz  
160 molecules<sup>32</sup>. The mixed sample exhibited significant improvements in terms of SAM uniformity  
161 and coverage: A consistent thickness was recorded for the mixed SAM on the same facet, albeit

162 with variations between 1 and 2 nm across different facets. Correspondingly, mixed SAM-  
163 modified FTO substrates exhibited higher hydrophobicity than control SAM-modified  
164 counterparts (Supplementary Fig. 15). Cyclic voltammetry (CV) measurements further determined  
165 the areal density of 2PACz in the mixed SAM to be  $3.9 \times 10^{13}$  molecules  $\text{cm}^{-2}$ , a 70% increase  
166 from the  $2.3 \times 10^{13}$  molecules  $\text{cm}^{-2}$  in the control SAM (Supplementary Fig. 16)<sup>16,27</sup>.

### 167 **Characterization of perovskite films**

168 To investigate the impact of SAMs on the structural and optoelectronic properties of perovskites,  
169 we fabricated triple-cation  $\text{Cs}_{0.05}\text{MA}_{0.10}\text{FA}_{0.85}\text{PbI}_3$  perovskite thin films on different FTO/SAM  
170 substrates. From scanning electron microscopy (SEM), we observed no notable change in the  
171 perovskite surface morphology when 3-MPA was incorporated into the SAM (Fig. 3a, b). Grazing  
172 incidence wide-angle x-ray scattering (GIWAXS) measurements showed nearly identical crystal  
173 structures for perovskites deposited on both the control and mixed SAMs (Fig. 3c). Here, the main  
174 constituent was photoactive  $\alpha$ -phase perovskites, with traces of the 4H hexagonal phase detected  
175 at  $q = 0.82 \text{ \AA}^{-1}$  and  $0.92 \text{ \AA}^{-1}$  as well as  $\text{PbI}_2$  at  $q = 0.90 \text{ \AA}^{-1}$ , respectively (Supplementary Fig. 14)<sup>33</sup>.  
176 Time-of-flight secondary ion mass spectrometry (TOF-SIMS) further confirmed that both 3-MPA  
177 and 2PACz molecules, due to their chemisorption on FTO surfaces, remained localized at the  
178 perovskite/FTO interfaces (Fig. 3d, e). These findings suggest that 3-MPA is not likely to change  
179 the perovskite formation process or contribute to the grain boundary or top surface passivation.

180 We conducted photoluminescence (PL) characterization by exciting perovskite thin films at a 1-  
181 sun-equivalent photon flux. We saw an average photoluminescence quantum yield (PLQY) of  $0.13\% \pm 0.02\%$   
182 for perovskites directly deposited onto FTO substrates, corresponding to a quasi-Fermi  
183 level splitting (QFLS) of 1.105 eV (Supplementary Table 1)<sup>34</sup>. 2PACz can passivate defects on  
184 metal oxide surfaces and effectively block electron injection<sup>35</sup>, resulting in an approximately 50-  
185 fold increase in the PL intensity (Fig. 3f). We noted an average PLQY of  $7\% \pm 2\%$  for the  
186 perovskite/2PACz/FTO stacks (Fig. 3g), corresponding to a QFLS of 1.207 eV. The incorporation  
187 of 3-MPA further improved the average PLQY to  $10\% \pm 1\%$ . This we ascribed to better SAM  
188 coverage rather than 3-MPA passivation since the thiol group of 3-MPA was embedded within the  
189 SAM (Fig. 1f).

190 We used ultraviolet and inverse photoelectron spectroscopy (UPS and IPES) to determine the work  
191 function and transport energy levels of perovskites and SAMs. The secondary electron cutoff in

192 the UPS spectra indicated an increase in the work function (WF) from 4.56 to 4.93 eV upon  
193 depositing the control SAM on the FTO substrate (Supplementary Fig. 18). 3-MPA led to an  
194 additional WF shift of +100 meV. The ionization energy (IE) was 5.51 and 5.64 eV for the control  
195 and mixed SAMs, respectively. In contrast, perovskites exhibited similar conduction band  
196 minimum (CBM) and valance band maximum (VBM) on different substrates (Fig. 3h). The  
197 resultant energy level diagrams of perovskites and SAMs are depicted in Fig. 3i, j. A vacuum level  
198 (VL) shift of 0.17 eV was recorded between the perovskite and the 2PACz bilayer, which further  
199 increased to 0.32 eV for the perovskite/mixed-SAM bilayer<sup>36</sup>. A higher VL shift indicates an  
200 enlarged built-in field<sup>37</sup>, which in PSCs can lead to enhanced carrier extraction<sup>38</sup>. Meanwhile, the  
201 IE offset between the bilayer remained consistent for the control and mixed SAMs (referenced to  
202 the Fermi level ( $E_F$ )).

### 203 **Solar cell efficiency and stability**

204 We fabricated PSCs having the inverted structure: FTO/SAM/perovskites/3,4,5-trifluoroanilinium  
205 (345FAn)/fullerene ( $C_{60}$ )/bathocuproine (BCP)/Ag (Fig. 4a and Supplementary Fig. 19). 345FAn  
206 was selected for interface engineering due to its thermal stability<sup>1</sup>. 2PACz (control) and 2PACz:3-  
207 MPA (mixed) were employed as the SAMs for hole-selective contact. The corresponding solar  
208 cell parameters are summarized in Fig. 4b. We found that compared to control devices, the mixed  
209 SAM led to improved performance (average PCE 25.0% compared with 24.1%). This came from  
210 open-circuit voltage ( $V_{oc}$ , from 1.141 V to 1.159 V) and fill factor (FF, from 82.3% to 84.1%)  
211 (Supplementary Note 4). We noted that device reproducibility was comparable for both control  
212 and mixed SAMs, likely due to SAM inhomogeneity occurring at the nanoscale<sup>18,27</sup>. The champion  
213 device with the mixed SAM exhibited a PCE of 25.3% from the reverse  $J$ - $V$  scan, which agrees  
214 with the PCE obtained from the steady-state power output (Supplementary Fig. 20). The integrated  
215 short-circuit current density ( $J_{sc}$ ) of 25.8 mA cm<sup>-2</sup> derived from the external quantum efficiency  
216 (EQE) measurement matches well with that from the  $J$ - $V$  sweep (Fig. 4c).

217 One mixed-SAM-based FTO device was characterized at Newport (Montana, USA); and produced  
218 a QSS-certified PCE of 24.8%, with a  $V_{oc}$  of 1.150 V, a  $J_{sc}$  of 25.5 mA cm<sup>-2</sup>, and an FF of 84.5%  
219 (Fig. 4d and Supplementary Fig. 21). Although there have been reports of inverted PSCs with  
220 efficiencies surpassing 25%<sup>2,3</sup>, the certified PCEs measured under stabilized conditions (including  
221 maximum power point (MPP) and QSS tracking) have yet to reach the same level (Supplementary

222 Table 2). The QSS efficiency reported herein represents a new record for inverted PSCs, improving  
223 upon the previous record QSS efficiency of 24.09% in literature (Fig. 4e).

224 For comparison, inverted PSCs were fabricated on smooth ITO substrates. We obtained an average  
225 PCE of 23.4% for control ITO devices, which was lower than that of control FTO devices, despite  
226 their higher average  $V_{oc}$  and FF (Supplementary Fig. 22). This emphasizes the need to augment  $J_{sc}$   
227 for inverted PSCs. The limited  $J_{sc}$  is ascribed to the smoothness of ITO substrates (Supplementary  
228 Fig. 23), leading to reduced light-scattering and thus insufficient light absorption in the full device  
229 (Supplementary Fig. 24). Interestingly, the performance of mixed-SAM-based ITO devices was  
230 only slightly improved, possibly due to the weak interactions of 3-MPA with ITO surfaces  
231 (Supplementary Note 5; Supplementary Fig. 25).

232 We evaluated the operating stability of PSCs using International Summit on Organic Photovoltaic  
233 Stability (ISOS)-L-3 protocols, in which the encapsulated device was subjected to continuous 1-  
234 sun equivalent, white-LED illumination (Supplementary Fig. 26) at 50% relative humidity and  
235 heatsink temperature of 65°C. To impede ion and moisture diffusion, we replaced BCP with  
236 atomic-layer-deposited SnO<sub>2</sub> as a buffer layer<sup>9</sup>. The resultant device delivered a PCE of 24.6% at  
237 room temperature (Supplementary Fig. 27). During the ISOS-L-3 testing, the device initially  
238 demonstrated a PCE of 22.6%, which increased to 23.1% after 1.6 hours of MPP tracking (Fig. 4f).  
239 The lower PCE at 65°C, compared to room temperature, is ascribed to the negative temperature  
240 coefficient of PSCs ( $-0.15\% / ^\circ\text{C}$ )<sup>39</sup>. The PCE stabilized at 21.9% (95% of the peak PCE) until the  
241 end of the test (1075 h), with the main degradation in the photocurrent (Supplementary Fig. 28).  
242 The initial performance and operating stability reported herein are compared with other PSCs  
243 subjected to ISOS-L-3 tests (Supplementary Table 3).

## 244 References

- 245 1. Park, S. M. *et al.* Engineering ligand reactivity enables high-temperature operation of  
246 stable perovskite solar cells. *Science* **381**, 209–215 (2023).
- 247 2. Zhang, S. *et al.* Minimizing buried interfacial defects for efficient inverted perovskite solar  
248 cells. *Science* **380**, 404–409 (2023).
- 249 3. Jiang, Q. *et al.* Surface reaction for efficient and stable inverted perovskite solar cells.  
250 *Nature* **611**, 278–283 (2022).
- 251 4. Kim, M. *et al.* Conformal quantum dot–SnO<sub>2</sub> layers as electron transporters for efficient  
252 perovskite solar cells. *Science* **375**, 302–306 (2022).



- 253 5. Park, J. *et al.* Controlled growth of perovskite layers with volatile alkylammonium chlorides.  
254 *Nature* **616**, 724–730 (2023).
- 255 6. Best Research-Cell Efficiency Chart. *NREL* <https://www.nrel.gov/pv/cell-efficiency.html>  
256 (2023).
- 257 7. You, S. *et al.* Radical polymeric p-doping and grain modulation for stable, efficient  
258 perovskite solar modules. *Science* **379**, 288–294 (2023).
- 259 8. Zheng, X. *et al.* Managing grains and interfaces via ligand anchoring enables 22.3%-  
260 efficiency inverted perovskite solar cells. *Nat. Energy* **5**, 131–140 (2020).
- 261 9. Chen, H. *et al.* Quantum-size-tuned heterostructures enable efficient and stable inverted  
262 perovskite solar cells. *Nat. Photonics* **16**, 352–358 (2022).
- 263 10. Li, Z. *et al.* Organometallic-functionalized interfaces for highly efficient inverted perovskite  
264 solar cells. *Science* **376**, 416–420 (2022).
- 265 11. Peng, W. *et al.* Reducing nonradiative recombination in perovskite solar cells with a porous  
266 insulator contact. *Science* **379**, 683–690 (2023).
- 267 12. Camaioni, N. *et al.* Polymer solar cells with active layer thickness compatible with scalable  
268 fabrication processes: a meta-analysis. *Adv. Mater.* **35**, 2210146 (2023).
- 269 13. Sahli, F. *et al.* Fully textured monolithic perovskite/silicon tandem solar cells with 25.2%  
270 power conversion efficiency. *Nat. Mater.* **17**, 820–826 (2018).
- 271 14. Al-Ashouri, A. *et al.* Conformal monolayer contacts with lossless interfaces for perovskite  
272 single junction and monolithic tandem solar cells. *Energy. Environ. Sci.* **12**, 3356–3369  
273 (2019).
- 274 15. Paniagua, S. A. *et al.* Phosphonic acids for interfacial engineering of transparent conductive  
275 oxides. *Chem. Rev.* **116**, 7117–7158 (2016).
- 276 16. Truong, M. A. *et al.* Tripodal triazatruxene derivative as a face-on oriented hole-collecting  
277 monolayer for efficient and stable inverted perovskite solar cells. *J. Am. Chem. Soc.* **145**,  
278 7528–7539 (2023).
- 279 17. Isikgor, F. H. *et al.* Molecular engineering of contact interfaces for high-performance  
280 perovskite solar cells. *Nat. Rev. Mater.* **8**, 89–108 (2022).
- 281 18. Mao, L. *et al.* Fully textured, production-line compatible monolithic perovskite/silicon  
282 tandem solar cells approaching 29% efficiency. *Adv. Mater.* **34**, 1–12 (2022).
- 283 19. He, R. *et al.* Improving interface quality for 1-cm<sup>2</sup> all-perovskite tandem solar cells. *Nature*  
284 **618**, 80–86 (2023).
- 285 20. Phung, N. *et al.* Enhanced self-assembled monolayer surface coverage by ALD NiO in p-i-  
286 n perovskite solar cells. *ACS Appl. Mater. Interfaces* **14**, 2166–2176 (2022).
- 287 21. Farag, A. *et al.* Evaporated self-assembled monolayer hole transport layers: lossless  
288 interfaces in p-i-n perovskite solar cells. *Adv. Energy Mater.* **13**, 2203982 (2023).

- 289 22. Boyd, C. C. *et al.* Overcoming redox reactions at perovskite-nickel oxide interfaces to boost  
290 voltages in perovskite solar cells. *Joule* **4**, 1759–1775 (2020).
- 291 23. Fukano, T. Low-temperature growth of highly crystallized transparent conductive fluorine-  
292 doped tin oxide films by intermittent spray pyrolysis deposition. *Sol. Energy Mater Sol.*  
293 *Cells* **82**, 567–575 (2004).
- 294 24. Neale, N. R., Kopidakis, N., van de Lagemaat, J., Grätzel, M. & Frank, A. J. Effect of a  
295 coadsorbent on the performance of dye-sensitized tio<sub>2</sub> solar cells: shielding versus band-  
296 edge movement. *J. Phys. Chem. B* **109**, 23183–23189 (2005).
- 297 25. Deng, X. *et al.* Co-assembled monolayers as hole-selective contact for high-performance  
298 inverted perovskite solar cells with optimized recombination loss and long-term stability.  
299 *Angew. Chem. Int. Ed.* **134**, (2022).
- 300 26. Al-Ashouri, A. *et al.* Wettability improvement of a carbazole-based hole-selective  
301 monolayer for reproducible perovskite solar cells. *ACS Energy Lett.* **8**, 898–900 (2023).
- 302 27. Liu, M. *et al.* Compact hole-selective self-assembled monolayers enabled by disassembling  
303 micelles in solution for efficient perovskite solar cells. *Adv. Mater.* (2023)  
304 doi:10.1002/adma.202304415.
- 305 28. Love, J. C., Estroff, L. A., Kriebel, J. K., Nuzzo, R. G. & Whitesides, G. M. Self-assembled  
306 monolayers of thiolates on metals as a form of nanotechnology. *Chem. Rev.* **105**, 1103–  
307 1170 (2005).
- 308 29. Paniagua, S. A. *et al.* Phosphonic acid modification of indium–tin oxide electrodes:  
309 combined XPS/UPS/contact angle studies. *J. Phys. Chem. C* **112**, 7809–7817 (2008).
- 310 30. Hotchkiss, P. J., Malicki, M., Giordano, A. J., Armstrong, N. R. & Marder, S. R.  
311 Characterization of phosphonic acid binding to zinc oxide. *J. Mater. Chem.* **21**, 3107 (2011).
- 312 31. Nazeeruddin, M. K., Humphry-Baker, R., Liska, P. & Grätzel, M. Investigation of sensitizer  
313 adsorption and the influence of protons on current and voltage of a dye-sensitized  
314 nanocrystalline TiO<sub>2</sub> solar cell. *J. Phys. Chem. B* **107**, 8981–8987 (2003).
- 315 32. Bunker, B. C. *et al.* The impact of solution agglomeration on the deposition of self-  
316 assembled monolayers. *Langmuir* **16**, 7742–7751 (2000).
- 317 33. Dang, H. X. *et al.* Multi-cation synergy suppresses phase segregation in mixed-halide  
318 perovskites. *Joule* **3**, 1746–1764 (2019).
- 319 34. Caprioglio, P. *et al.* On the relation between the open-circuit voltage and quasi-fermi level  
320 splitting in efficient perovskite solar cells. *Adv. Energy Mater.* **9**, 1901631 (2019).
- 321 35. Al-Ashouri, A. *et al.* Monolithic perovskite/silicon tandem solar cell with >29% efficiency  
322 by enhanced hole extraction. *Science* **370**, 1300–1309 (2020).
- 323 36. Li, X. *et al.* Mapping the energy level alignment at donor/acceptor interfaces in non-  
324 fullerene organic solar cells. *Nat. Commun.* **13**, 2046 (2022).
- 325 37. Lami, V. *et al.* Visualizing the vertical energetic landscape in organic photovoltaics. *Joule*  
326 **3**, 2513–2534 (2019).

- 327 38. Sandberg, O. J. *et al.* On the question of the need for a built-in potential in perovskite solar  
328 cells. *Adv. Mater. Interfaces* **7**, 2000041 (2020).
- 329 39. Moot, T. *et al.* Temperature coefficients of perovskite photovoltaics for energy yield  
330 calculations. *ACS Energy Lett.* **6**, 2038–2047 (2021).

ACCELERATED ARTICLE PREVIEW

331 **Figure Legends**

332 **Fig.1|MD simulations of phosphonic acid adsorption with and without molecular additives.**  
333 **a**, Chemical structures of the phosphonic acid 2PACz and the bifunctional compound 3-MPA. **b**,  
334 Total number of 2PACz clusters formed over a set period, in the absence (control) and presence  
335 (mixed) of 3-MPA. **c**, Types of 2PACz clusters formed at equilibrium. **d**, **e**, Top views of  
336 equilibrated molecular representations of control (**d**) and mixed (**e**) systems. 2PACz and 3-MPA  
337 (where applicable) are shown in pink and blue, respectively; Sn and O atoms, shown in the  
338 background, are depicted in yellow and red, respectively. **f**, Successive steps along an AIMD  
339 trajectory showcasing the role of 3-MPA as a co-adsorbent. Large, encircled areas are  
340 magnifications of small ones.

341 **Fig.2|Homogeneity of self-assembled monolayers formed on FTO substrates.** **a**, XPS P 2*p* (left)  
342 and S 2*p* (right) spectra for the control and mixed samples. The peaks were fitted using one S 2*p*  
343 or P 2*p* doublet with a 2:1 peak area ratio. **b**, 2PACz (left) and 3-MPA (right) transmission FTIR  
344 spectra, compared with ATR-FTIR spectra for the SAM (left) and 3-MPA (right) coated FTO  
345 substrates. The FTIR peaks identified at 947 and 1021 cm<sup>-1</sup> for 2PACz powders correspond to the  
346 symmetric and asymmetric stretching of P–OH, respectively. Cz = carbazole. **c**, KPFM images of  
347 control (left) and mixed (right) SAM-coated FTO substrates. **d**, Cross-sectional HAADF-STEM  
348 images of control (top) and mixed (bottom) SAMs sandwiched between MoO<sub>x</sub> and FTO.

349 **Fig.3|Materials properties of perovskite films on different FTO/SAM substrates.** **a**, **b**, Top-  
350 view SEM images of perovskite films deposited on control (**a**) and mixed (**b**) SAMs. **c**, GIWAXS  
351 images for perovskite films on control (left) and mixed (right) SAMs. The color bar shows the  
352 diffraction intensity collected from the GIWAXS detector.  $q_{xy}$  and  $q_z$  represent in-plane and near  
353 out-of-plane scattering vectors, respectively. **d**, **e**, TOF-SIMS profiles of perovskites on  
354 FTO/control SAM (**d**) and FTO/mixed SAM (**e**) substrates measured in negative polarity. Traces  
355 of SH<sup>-</sup> were identified at the perovskite/control SAM interface, possibly due to contamination of  
356 precursor materials. **f**, Absolute intensity PL spectra of perovskite films on bare FTO (no SAM)  
357 and control and mixed SAMs. **g**, PLQYs of perovskite films on control and mixed SAMs (5  
358 samples for each condition). Statistical distribution represented in box plots (line within the box:  
359 mean, box limit: standard deviation). **h**, UPS and IPES spectra of perovskite films on control and  
360 mixed SAMs. Gaussian fit (grey line) was used to determine the conduction and valence bands. **i**,  
361 **j**, Schematic energy level diagrams of the perovskite/control SAM (**i**) and perovskite/mixed SAM  
362 bilayer (**j**), respectively.

363 **Fig.4|Photovoltaic performance of perovskites solar cells.** **a**, Schematic illustration of the  
364 device architecture with textured FTO substrate. **b**, Solar cell parameters for the control (16 devices)  
365 and mixed (32 devices) SAM devices. Statistical distribution represented in box-and-whisker plots  
366 (line within box: median, box limit: standard deviation, whiskers: 1.5 outliers). **c**, EQE and  
367 integrated  $J_{sc}$  (grey dashed line) curves of the mixed SAM device. **d**, QSS  $J$ - $V$  curve of one  
368 representative mixed SAM device certified at Newport. Inset: PV parameters of the device. **e**,  
369 Certified performance of inverted PSCs measured under the QSS condition. **f**, MPP tracking of the  
370 encapsulated mixed SAM device at heatsink temperature of 65°C with a relative humidity of ~50%  
371 under 1-sun illumination. The device configuration is FTO/SAM/Perovskite/345FAn/C<sub>60</sub>/ALD-  
372 SnO<sub>2</sub>/Ag, having a PCE of 24.6% at room temperature.

## 373 **Methods**

### 374 **Molecular dynamics simulations**

375 Static DFT calculation and AIMD were performed with the CP2K<sup>40</sup> package utilizing a mixed  
376 Gaussian/plane wave (GPW) basis. The PBE exchange-correlation functional<sup>41</sup>, DFT-D3  
377 dispersion corrections<sup>42</sup>, and dipole corrections<sup>43</sup> necessary for periodic boundary conditions along  
378 the perpendicular direction to the surface were included. Valence electron wave functions were  
379 expanded in a double- $\zeta$  Gaussian basis set with polarization functions (DZVP)<sup>44</sup>. The energy cut-  
380 off for the electron density expansion in the GPW method was 400 Ry. Born-Oppenheimer AIMD  
381 simulations were run with an integration time step of 0.5 fs and the system was kept at 300 K using  
382 the thermostat of Bussi et al.<sup>45</sup> in a canonical isothermal-isochoric (NVT) ensemble, where the  
383 total number of atoms  $N$ , the volume  $V$  and the temperature  $T$  of the system were held constant.  
384 All AIMD simulations were performed at  $\Gamma$  point. Being the most stable surface, the SnO<sub>2</sub> (110)  
385 was chosen as the substrate surface. The systems were equilibrated over 5 ps in the NVT ensemble  
386 and the remaining 40 ps were used for the production run. To investigate the interactions between  
387 the 2PACz and 3-MPA molecules, as well as molecules and the SnO<sub>2</sub> substrate, 5 scenarios were  
388 simulated: (1) a single molecule (2PACz or 3-MPA) on SnO<sub>2</sub> (110), (2) one 2PACz and one 3-  
389 MPA concurrently on SnO<sub>2</sub> (110), (3) two 2PACz and one 3-MPA on SnO<sub>2</sub>(110), (4) four 2PACz  
390 and one 3-MPA on SnO<sub>2</sub>(110), and (5) six 2PACz and one 3-MPA on SnO<sub>2</sub> (110). In all the  
391 scenarios, an in-plane SnO<sub>2</sub> (110) simulation cell of 22.690 Å × 27.756 Å with 45 Å of vacuum  
392 between the slab repetitions was used. AIMD was also used to estimate the interaction energy of  
393 2PACz and 3-MPA with the SnO<sub>2</sub> (110) surface. The final AIMD configurations were relaxed with  
394 DFT to extract the interaction energies of the molecules. Binding energies were calculated as  
395  $\Delta E_b = E_{\text{tot}} - E_s - E_{\text{mol}}$ , where  $E_{\text{tot}}$  is the energy of the final relaxed configuration (molecule on  
396 SnO<sub>2</sub> (110));  $E_s$  is the energy of the final configuration of the slab;  $E_{\text{mol}}$  is the energy of the final  
397 configuration of the isolated molecule. The interaction energies of 2PACz clusters were computed  
398 after DFT relaxations of isolated clusters. Dimers, trimers, and tetramers were considered.  
399 Interaction energies per molecule were calculated as  $\Delta E_i = (E_{\text{tot}} - nE_{\text{mol}})/n$ , where  $E_{\text{tot}}$  is the energy  
400 of the final relaxed cluster;  $n$  is the number of molecules forming the cluster;  $E_{\text{mol}}$  is the energy of  
401 a single relaxed molecule assumed isolated. Vibrational power spectra were computed as the  
402 Fourier transform of the autocorrelation function of the atomic velocities.

403 Classical MD simulations with full atomic resolution were realized with the help of the LAMMPS  
404 MD simulator<sup>46</sup>. The equations of motion were integrated using the Velocity-Verlet method<sup>47</sup>, with  
405 a 1 fs time step, while bond stretching was not constrained for any bonds. To maintain isothermal  
406 conditions, the deterministic Nosé – Hoover thermostat<sup>48,49</sup>, with a time constant equal to 0.1 ps,  
407 was utilized. This ensured that thermostating was applied to both translational and rotational  
408 degrees of freedom, crucial for the asymmetric 2PACz and 3-MPA molecules. All classical MD  
409 simulations were realized in the canonical NVT ensemble at  $T = 300\text{K}$  comprising a V-shaped  
410 SnO<sub>2</sub> (110) model system with dimensions 60 Å × 105 Å × 40 Å. Periodic boundary conditions  
411 were used in x- and y-directions, whereas reflective boundary conditions were employed in the z-  
412 direction. The two considered systems, control and mixed, comprised a total of 18498 and 18714  
413 atoms, respectively, whereas the experimental molar ratio (2PACz/3-MPA= 9/1) was retained in  
414 the simulated mixed system. The systems were equilibrated for 1 ns followed by a 10ns production  
415 simulation, where sampling took place every 500 fs for the calculation of ensemble averages. A  
416 snapshot of the system was taken every 1000 fs for visualization purposes. The calculation of the  
417 number distributions of formed 2PACz clusters was performed through an in-house code utilizing

418 a threshold distance of 8 Å among the centre of masses of adjacent 2PACz molecules in accordance  
419 with the nearest neighbour shell of the corresponding radial distribution function as clustering  
420 criterion.

421 To accurately capture the interactions of SnO<sub>2</sub>, the thoroughly validated classical force field  
422 developed by Bandura et al.<sup>50</sup> was used. The all-atom OPLS force field was utilized for 3-MPA,  
423 wherein the corresponding interaction parameters were obtained with the help of the LigParGen  
424 server<sup>51</sup>. For 2PACz, containing the phosphonic functional group, the specially designed force field  
425 developed by Meltzer et al.<sup>52</sup> based on the Generalized Amber Force Field<sup>53</sup> was utilized. The van  
426 der Waals and electrostatic non-bonded interactions were calculated using a real-space cutoff  
427 radius of 10 Å and 8 Å, respectively, whereas the particle-particle-particle-mesh (PPPM) scheme<sup>54</sup>  
428 with an accuracy of 0.0001 (kcal/mol)/Å was used for the consideration of long-range electrostatic  
429 interactions. Because the SnO<sub>2</sub> force field uses a Buckingham potential for the van der Waals  
430 interactions, its combination with the Lennard-Jones potential used for the compounds was  
431 realized by fitting the Buckingham parameters of SnO<sub>2</sub> to a suitable set of Lennard-Jones  
432 parameters<sup>55</sup> and geometric mixing rules were applied for all dissimilar non-bonded interactions.

### 433 **Materials**

434 All materials were used as received without further purification. Organic halide salts, including  
435 methylammonium iodide (MAI), formamidinium iodide (FAI), methylammonium chloride  
436 (MACl), were purchased from Great Cell Solar. Cesium iodide (CsI), 3-mercaptopropionic acid  
437 (3-MPA), 3,4,5-trifluoroaniline (98%), and guanidinium thiocyanate (GuaSCN) were purchased  
438 from Sigma-Aldrich. 3,4,5-trifluoroaniline was converted to its ammonium form following the  
439 published procedure. [2-(9H-Carbazol-9-yl)ethyl]phosphonic Acid (2PACz), lead iodide (PbI<sub>2</sub>,  
440 99.99%), and bathocuproine (BCP) were purchased from TCI. Anhydrous solvents including N,  
441 N-dimethylformamide (DMF, 99.8%), dimethyl sulfoxide (DMSO, 99.9%), 2-propanol (IPA,  
442 99.5%), chloroform (CF, 99.8%), and anisole (99.7%) were purchased from Sigma-Aldrich. C<sub>60</sub>  
443 was purchased from Xi'an Polymer Light Technology Corp. ITO and FTO (TEC 10) substrates  
444 were purchased from Thin Film Devices Inc. and Ossila, respectively.

### 445 **Perovskite film fabrication**

446 1.5 M of Cs<sub>0.05</sub>MA<sub>0.1</sub>FA<sub>0.85</sub>PbI<sub>3</sub> perovskite precursor was fully dissolved in mixed solvents of DMF  
447 and DMSO (4:1, v/v) with the molar ratio for FAI/MAI/CsI was 0.85:0.1:0.05. 10 mg mL<sup>-1</sup> MACl  
448 and 8 mg mL<sup>-1</sup> GuaSCN were added in the solution to improve the film morphology. The precursor  
449 solution was filtered through a 0.22 μm polytetrafluoroethylene (PTFE) membrane before use. 60  
450 μL of perovskite solution was deposited on the substrate and spun cast at 1000 rpm for 10 s  
451 followed by 6000 rpm for 30 s. 150 μL anisole was dropped onto the substrate during the last 5 s  
452 of the spinning, resulting in the formation of dark brown films that were then annealed on a hot  
453 plate at 100°C for ITO and 120°C for FTO for 20 min.

### 454 **Device fabrication**

455 FTO glasses were sequentially sonicated in aqueous detergent, deionized water, acetone, and IPA  
456 each for 10 min. After drying with nitrogen, the substrates were exposed to UV-ozone treatment  
457 for 15 min to remove organic contaminants and then transferred into a nitrogen-filled glovebox  
458 maintaining less than 0.1 ppm of O<sub>2</sub> and H<sub>2</sub>O. 100 μL of 2PACz or a mixture of 2PACz:3-MPA (in  
459 a molar ratio of either 9:1 in characterization and device fabrication, or 8:2 in XPS measurements)

460 in anhydrous ethanol (1 mM) solution was uniformly spread on the substrates and allowed to rest  
461 for 15 s, followed by spinning the films at 3000 rpm for 30s. The films were then annealed at  
462 100°C for 10 min and washed by dropping 500  $\mu\text{L}$  ethanol during the film spinning at 3000 rpm.  
463 Perovskites solution was deposited on the SAM-modified substrate as detailed above. 200  $\mu\text{L}$  of  
464 345FAn solution (1 mg/mL) in CF with an additional 3% of IPA was then drop cast within 2-3 s  
465 on the perovskite film spinning at 4000 rpm (i.e., dynamic spinning) and annealed at 100°C for 5  
466 min. Both control and mixed SAM films were then transferred to the thermal evaporator  
467 (Angstrom engineering).  $\text{C}_{60}$  (30 nm) and BCP (7 nm) were deposited sequentially with a rate of  
468  $0.3 \text{ \AA s}^{-1}$  and  $0.5 \text{ \AA s}^{-1}$ , respectively, at a pressure of ca.  $2 \times 10^{-6}$  mbar. Finally, Ag contact (140  
469 nm) was deposited on top of BCP through a shadow mask with the desired aperture area. For the  
470 stability testing, ALD- $\text{SnO}_2$  were used as the barrier layer. The deposition of ALD- $\text{SnO}_2$  was  
471 carried out in the PICOSUN R-200 Advanced ALD system.  $\text{H}_2\text{O}$  and  $\text{TDMASn}$  were used as  
472 oxygen and tin precursors. Precursor and substrate temperature were set to 75°C and 85°C,  
473 respectively. 90 SCCM  $\text{N}_2$  was used as carrier gas. Pulse and purge times for  $\text{H}_2\text{O}$  were 1 s and 5  
474 s, and 1.6 s and 5 s for  $\text{TDMASn}$ . The total deposition cycle is 120, corresponding to 20 nm of  
475  $\text{SnO}_2$ .

#### 476 **Solar cell characterization**

477 The current-voltage ( $I$ - $V$ ) characteristics of solar cells were measured using a Keithley 2400  
478 sourcemeter under the illumination of solar simulator (Newport, Class AAA) at the light intensity  
479 of  $100 \text{ mW cm}^{-2}$  as checked with a calibrated reference solar cell (Newport). The stabilized PCE  
480 was measured by setting the bias voltage to the  $V_{\text{MPP}}$  and then tracing the current density. The  $V_{\text{MPP}}$   
481 was determined from the reverse  $I$ - $V$  curve. The active area was determined by the aperture shade  
482 mask ( $0.049 \text{ cm}^2$ ) placed in front of the solar cell to avoid overestimation of the photocurrent  
483 density. EQE spectra were recorded with a commercial system (Arkeo-Ariadne, Cicci Research  
484 s.r.l.) based on a 300 W xenon light source and a holographic grating monochromator (Cornerstone,  
485 Newport).

#### 486 **Stability tests of solar cells**

487 Devices were placed in a homemade stability tracking station. The illumination source is a white  
488 light LED with intensity calibrated to match the 1-sun condition. For the ISOS-L-3 ageing protocol  
489 ( $65$  or  $85^\circ\text{C}$ ; 50% relative humidity; MPP)<sup>56</sup>, the device chamber was left open in a room with  
490  $50 \pm 10\%$  humidity and solar cell was mounted on a metal plate kept at  $65^\circ\text{C}$  by a heating element.  
491 A thermal couple attached to the metal plate was used to monitor and provide feedback control to  
492 the heating element to ensure temperature consistency. MPP was tracked using a home-build  
493 MATLAB-based MPP tracking system using a 'perturb and observe' method. The MPP was  
494 updated every 1000 minutes. Encapsulation was done by capping the device with a glass slide,  
495 using UV-adhesive (Lumtec LT-U001) as a sealant.

#### 496 **XPS measurements**

497 XPS measurements were performed with a Thermo Scientific K-Alpha system with  $180^\circ$  double-  
498 focusing, hemispherical analyser. The system is equipped with a 128-channel detector and  
499 monochromatic small spot XPS. An Al  $K\alpha$  source (1486.6 eV) was used for excitation and a pass  
500 energy of 50 eV was used for XPS acquisition. Samples mounted on a metal specimen holder. All  
501 data were analysed with CasaXPS and Thermo Advantage software.

## 502 **KPFM measurements**

503 KPFM measurements were performed using an Asylum Research Cypher S atomic force  
504 microscope (Oxford Instruments, Santa Barbara, USA) with an ASYELEC.01-R2 Ti-Ir coated  
505 cantilever (Asylum Research). Scans were performed over 2  $\mu\text{m}$  at 512 pixels and 0.5 Hz using a  
506 two-pass method where the first pass is a tapping mode topography scan and the second in KPFM  
507 mode with a tip potential of 3 V and a surface clearance of 5 nm. Cantilever calibration was  
508 performed using the Thermal method from the Asylum Research GetReal database.

## 509 **HAADF-TEM measurements**

510 HAADF-TEM images were acquired at an aberration corrected FEI (Titan Cubed Themis G2)  
511 operated at 300 kV equipped with an XFEG gun and Bruker Super-X EDS detectors. The SAM  
512 samples had a structure of glass/FTO/SAM/MoO<sub>x</sub> (50 nm), where the MoO<sub>x</sub> layer was deposited  
513 through thermal evaporation with a low rate of 0.1  $\text{\AA s}^{-1}$  at a pressure below  $2 \times 10^{-4}$  Pa. The cross-  
514 sectional samples were prepared by using a focused ion beam system (FIB, Helios G4 UX).  
515 Another protective layer of carbon was thermally evaporated before ion-beam cutting and etching.

## 516 **CV measurements**

517 CV measurements were conducted using a three-electrode configuration with a potentiostat  
518 (PGSTAT204, Autolab). The working electrodes were prepared using a spin coating method on  
519 an FTO electrode. The exposed area of the working electrode to the electrolyte measures 8 mm  $\times$   
520 21.4 mm. A platinum plate and an Ag/AgCl electrode (in a 3.0 M KCl solution) were employed  
521 as the counter and reference electrodes, respectively. The measurements were performed in an Ar-  
522 saturated solution of 1,2-dichlorobenzene (o-DCB) with 0.1 M tetrabutylammonium  
523 hexafluorophosphate (TBA<sup>+</sup>PF<sub>6</sub><sup>-</sup>) serving as the supporting electrolyte. All potentials are  
524 referenced against the ferrocene redox couple, serving as an internal standard. The effective  
525 coverage of the self-assembled monolayers on the FTO surface is measured by the slope of a linear  
526 dependency of the oxidative peak intensity against the scan rate as follows:

$$527 \quad i_{p,o} = \frac{n^2 F^2}{4RTN_A} A I^* v$$

528  $i_{p,o}$  is the oxidative peak current,  $v$  is the voltage scan rate,  $n$  is the number of electrons transferred,  
529  $F$  is the Faraday constant (96,485 C mol<sup>-1</sup>),  $R$  is the universal gas constant (8.314 J K<sup>-1</sup> mol<sup>-1</sup>),  $T$   
530 is the temperature,  $N_A$  is the Avogadro constant,  $A$  is the electrode area, and  $I^*$  is the areal density.

## 531 **UPS and IPES measurements**

532 UPS measurements were taken with an Excitech H Lyman- $\alpha$  photon source (10.2 eV) with a  
533 nitrogen-filled beam path coupled with a PHI 5600 UHV and analyser system. A sample bias of -  
534 5 V was applied and a pass energy of 5.85 eV was used for UPS acquisition. IPES measurements  
535 were performed in the Bremsstrahlung isochromatic mode with electron kinetic energies below 5  
536 eV and an electron gun emission current of 2  $\mu\text{A}$  was used to minimize sample damage. A Kimball  
537 Physics ELG-2 electron gun with a BaO cathode was used to generate the electron beam. Emitted  
538 photons were collected with a bandpass photon detector consisting of an optical bandpass filter  
539 (254 nm, Semrock) and a photomultiplier tube (R585, Hamamatsu Photonics). Samples were held  
540 at a -20 V bias during all IPES measurements and the UHV chamber was completely dark.



541 **Other characterizations**

542 Particle size distributions in solutions were determined by the DLS technique using a Malvern  
543 Zetasizer Nano ZS. Contact angles were measured using VCA-Optima XE. The image was taken  
544 with CCD camera within 1 s after water droplet. GIWAXS measurements were performed at CMS  
545 beamline, NSLS II. The monochromatic X-ray with the energy of 13.5 keV shone upon the  
546 samples at different grazing incident angles of 1°, 0.5°, and 0.08° with an exposure time of 10 s.  
547 A Pilatus800K detector was placed 259 mm away from the sample to capture the 2D diffraction  
548 pattern. Absolute intensity photoluminescence spectra were measured using an integrating sphere,  
549 and Andor Kymera 193i spectrograph, and a 660 nm continuous-wave laser set at 1-sun equivalent  
550 photon flux (1.1  $\mu\text{m}$  beam full-width half-maximum, 632  $\mu\text{W}$ ); photoluminescence was collected  
551 at normal incidence using a 0.1 NA, 110  $\mu\text{m}$ -diameter optical fiber. TOF-SIMS was conducted on  
552 the IONTOF M6 instrument with a  $\text{Bi}^{3+}$  (30 keV) primary ion beam for analysis and an Cs-cluster  
553 gun (2 keV) for sputtering. Data was acquired in positive mode with an analysis area of  $49 \times 49$   
554  $\mu\text{m}^2$  centred and a raster area of  $200 \times 200 \mu\text{m}^2$ . IR spectra were obtained in the attenuated total  
555 reflectance mode using a Fourier-transform IR spectrometer (Thermo Scientific iS50). Samples  
556 were prepared on the FTO substrate and scanned in the spectral range of 4000 to 550  $\text{cm}^{-1}$  with a  
557 minimum number of 500 scans and a resolution of 4  $\text{cm}^{-1}$ . The triangular apodization function was  
558 used to improve the signal-to-noise ratio. High-resolution SEM images were obtained using the  
559 Hitachi S5200 microscope with an accelerating voltage of 1.5 kV. A low accelerating voltage and  
560 a low beam current were deployed to reduce surface damage of perovskite films under electron  
561 beam bombardment. The diffuse and specular light reflected from the substrate surface was  
562 measured using a Cary 5000 UV-Vis-NIR double-beam spectrophotometer in diffuse reflectance  
563 mode. Pure  $\text{BaSO}_4$  was used for the baseline collection.

564 **Additional References**

- 565 40. Kühne, T. D. *et al.* CP2K: An electronic structure and molecular dynamics software package  
566 - Quickstep: Efficient and accurate electronic structure calculations. *J. Chem. Phys.* **152**,  
567 194103 (2020).
- 568 41. Van Setten, M. J. *et al.* The PseudoDojo: Training and grading a 85 element optimized  
569 norm-conserving pseudopotential table. *Comput. Phys. Commun.* **226**, 39–54 (2018).
- 570 42. Grimme, S. Density functional theory with London dispersion corrections. *Wiley Interdiscip.*  
571 *Rev. Comput. Mol. Sci.* **1**, 211–228 (2011).
- 572 43. Bengtsson, L. Dipole correction for surface supercell calculations. *Phys. Rev. B* **59**, 12301–  
573 12304 (1999).
- 574 44. VandeVondele, J. & Hutter, J. Gaussian basis sets for accurate calculations on molecular  
575 systems in gas and condensed phases. *J. Chem. Phys.* **127**, 114105 (2007).
- 576 45. Bussi, G., Donadio, D. & Parrinello, M. Canonical sampling through velocity rescaling. *J.*  
577 *Chem. Phys.* **126**, 014101 (2007).
- 578 46. Kryuchkov, N. P., Yurchenko, S. O., Fomin, Y. D., Tsiok, E. N. & Ryzhov, V. N. Complex  
579 crystalline structures in a two-dimensional core-softened system. *Soft Matter.* **14**, 2152–  
580 2162 (2018).

- 581 47. Swope, W. C., Andersen, H. C., Berens, P. H. & Wilson, K. R. A computer simulation  
582 method for the calculation of equilibrium constants for the formation of physical clusters of  
583 molecules: Application to small water clusters. *J. Chem. Phys.* **76**, 637–649 (1982).
- 584 48. Nosé, S. A unified formulation of the constant temperature molecular dynamics methods. *J.*  
585 *Chem. Phys.* **81**, 511–519 (1984).
- 586 49. Kassir, Y., Kupiec, M., Shalom, A. & Simchen, G. Cloning and mapping of CDC40, a  
587 *Saccharomyces cerevisiae* gene with a role in DNA repair. *Curr. Genet.* **9**, 253–257 (1985).
- 588 50. Bandura, A. V., Sofo, J. O. & Kubicki, J. D. derivation of force field parameters for SnO<sub>2</sub>  
589 –H<sub>2</sub>O surface systems from plane-wave density functional theory calculations. *J. Phys.*  
590 *Chem. B* **110**, 8386–8397 (2006).
- 591 51. Dodda, L. S., Cabeza de Vaca, I., Tirado-Rives, J. & Jorgensen, W. L. LigParGen web  
592 server: an automatic OPLS-AA parameter generator for organic ligands. *Nucleic Acids Res.*  
593 **45**, W331–W336 (2017).
- 594 52. Meltzer, C. *et al.* indentation and self-healing mechanisms of a self-assembled monolayer—  
595 a combined experimental and modeling study. *J. Am. Chem. Soc.* **136**, 10718–10727 (2014).
- 596 53. Wang, J., Wolf, R. M., Caldwell, J. W., Kollman, P. A. & Case, D. A. Development and  
597 testing of a general amber force field. *J. Comput. Chem.* **25**, 1157–1174 (2004).
- 598 54. Hockney, R. W. & Eastwood, J. W. *Computer Simulation Using Particles*. (CRC Press,  
599 2021). doi:10.1201/9780367806934.
- 600 55. Lim, T.-C. Alignment of Buckingham parameters to generalized Lennard-Jones potential  
601 functions. *Zeitschrift für Naturforschung A* **64**, 200–204 (2009).
- 602 56. Khenkin, M. V. *et al.* Consensus statement for stability assessment and reporting for  
603 perovskite photovoltaics based on ISOS procedures. *Nat. Energy* **5**, 35–49 (2020).

604

## 605 **Acknowledgements**

606 This research was made possible by the U.S. Department of the Navy, Office of Naval Research  
607 Grant (N00014-20-1-2572). This work was supported in part by Ontario Research Fund-Research  
608 Excellence program (ORF7-Ministry of Research and Innovation, Ontario Research Fund-  
609 Research Excellence Round 7). This work was also supported under award number OSR-  
610 CRG2020-4350.2. M.W. acknowledges funding from the European Union’s Horizon 2020  
611 Research and Innovation program under the Marie Skłodowska-Curie Grant Agreement No.  
612 101026353. T.H., H.R.A., and K.R.G. gratefully acknowledge funding from the National Science  
613 Foundation under award no. DMR-2102257. L.X. acknowledges support by National Natural  
614 Science Foundation of China (no. 61935016, 52173153) and the Electron Microscopy Laboratory  
615 of Peking University for the use of electron microscopes. M.G.K. acknowledges support by the

616 Office of Naval Research under award number N00014-20-1-2725. A.A. acknowledges support  
617 by the Office of Naval Research under award number N00014-20-1-2573. P.S. acknowledges the  
618 support of the Vanier Canada Graduate Scholarship. This work made use of the NUFAB and Keck-  
619 II facilities of Northwestern University's NUANCE Center, which has received support from the  
620 SHyNE Resource (NSF ECCS-2025633), the IIN, and Northwestern's MRSEC program (NSF  
621 DMR-1720139). We thank Damir Kopilovic for providing the LED spectrum and Jing Gao for  
622 assisting with the SEM measurements.

### 623 **Author contributions**

624 S.M.P., M.W., M.G., and E.H.S. conceived the idea and proposed the experimental and modelling  
625 design. N.L., L.A., V.C., and U.R. carried out the MD simulation. S.M.P. fabricated all the devices  
626 and conducted the characterization. T.H., H.R.A and K.R.G performed XPS, UPS, and IPES  
627 characterization and data analysis. W.Y. and L.X. carried out the HAADF-STEM measurements.  
628 F.T.E., M.W., S.M.Z., and M.G. conducted the PL and EQE characterization and data analysis.  
629 M.W. measured DLS. H.S. conducted CV measurements and data analysis. D.C. performed UV-  
630 Vis spectroscopy characterization. Y.Y. and M.G.K. measured TOF-SIMS. K.D. and A.A.  
631 performed the GIWAXS measurements. M.V., E.D.J. and D.B.K. helped with the device  
632 fabrication and material characterization. P.S. and T.F. performed the KPFM measurements. M.W.,  
633 S.M.P., N.L., M.G., and E.H.S. co-wrote the manuscript. All authors contributed to data analysis,  
634 read, and commented on the manuscript.

### 635 **Competing interests**

636 The authors declare no competing interests.

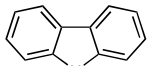
### 637 **Data availability**

638 All data are available in the main text or the supplementary materials. Further data are available  
639 from the corresponding author on reasonable request.

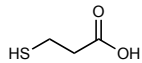
### 640 **Code availability**

641 The codes and post-analysis tools for MD simulations are available in the following repository:  
642 <https://doi.org/10.5281/zenodo.8393081>.

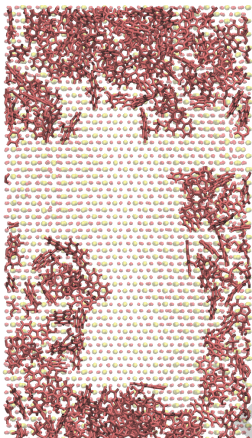
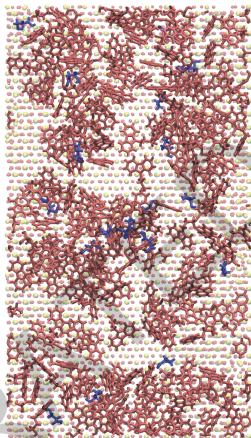
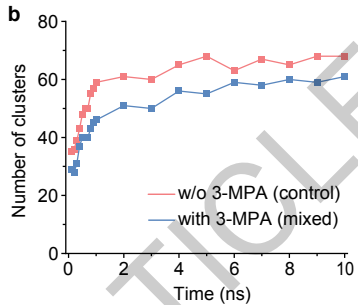
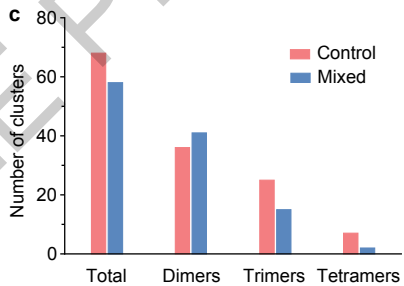
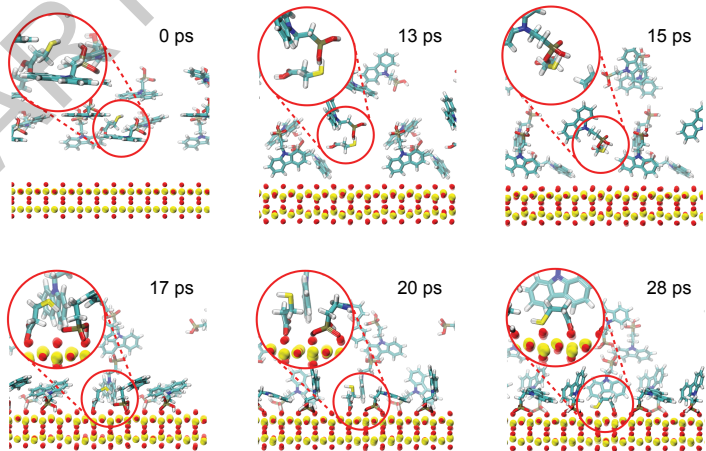
643 **Correspondence and requests for materials** should be addressed to M.G. or E.H.S.

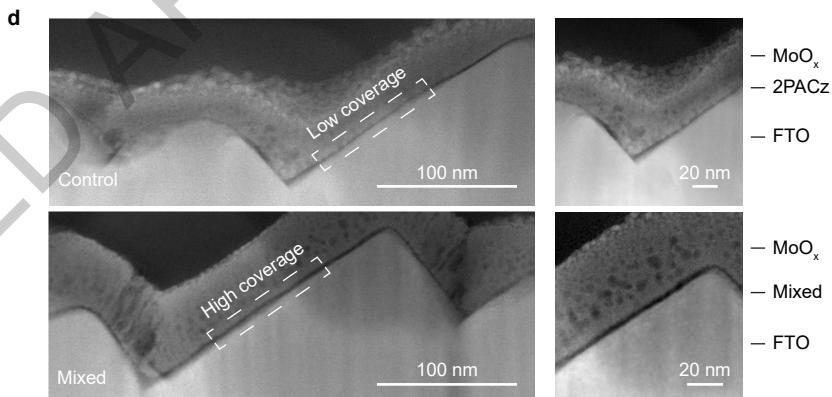
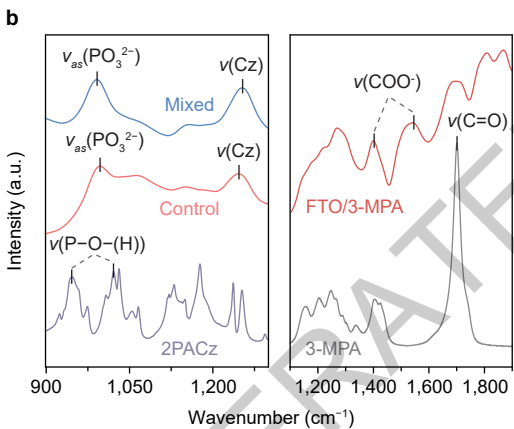
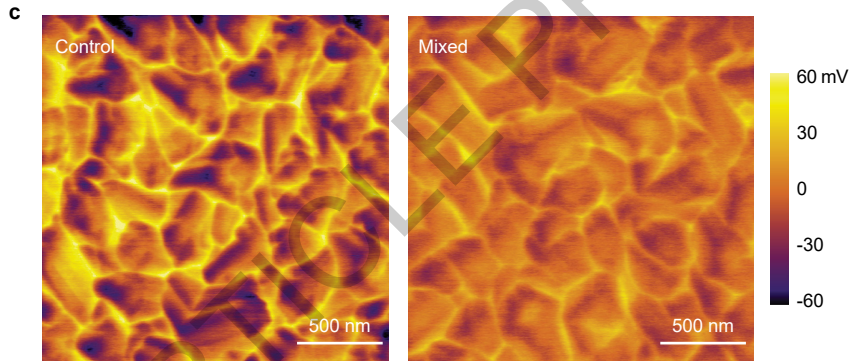
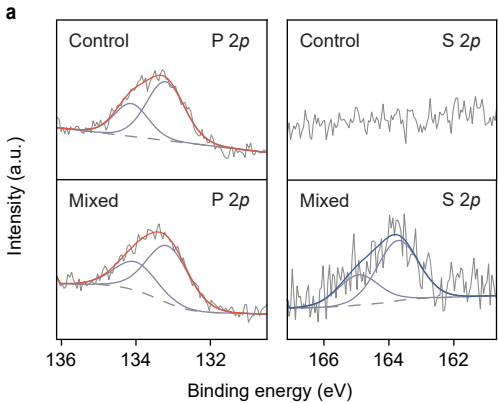
**a**

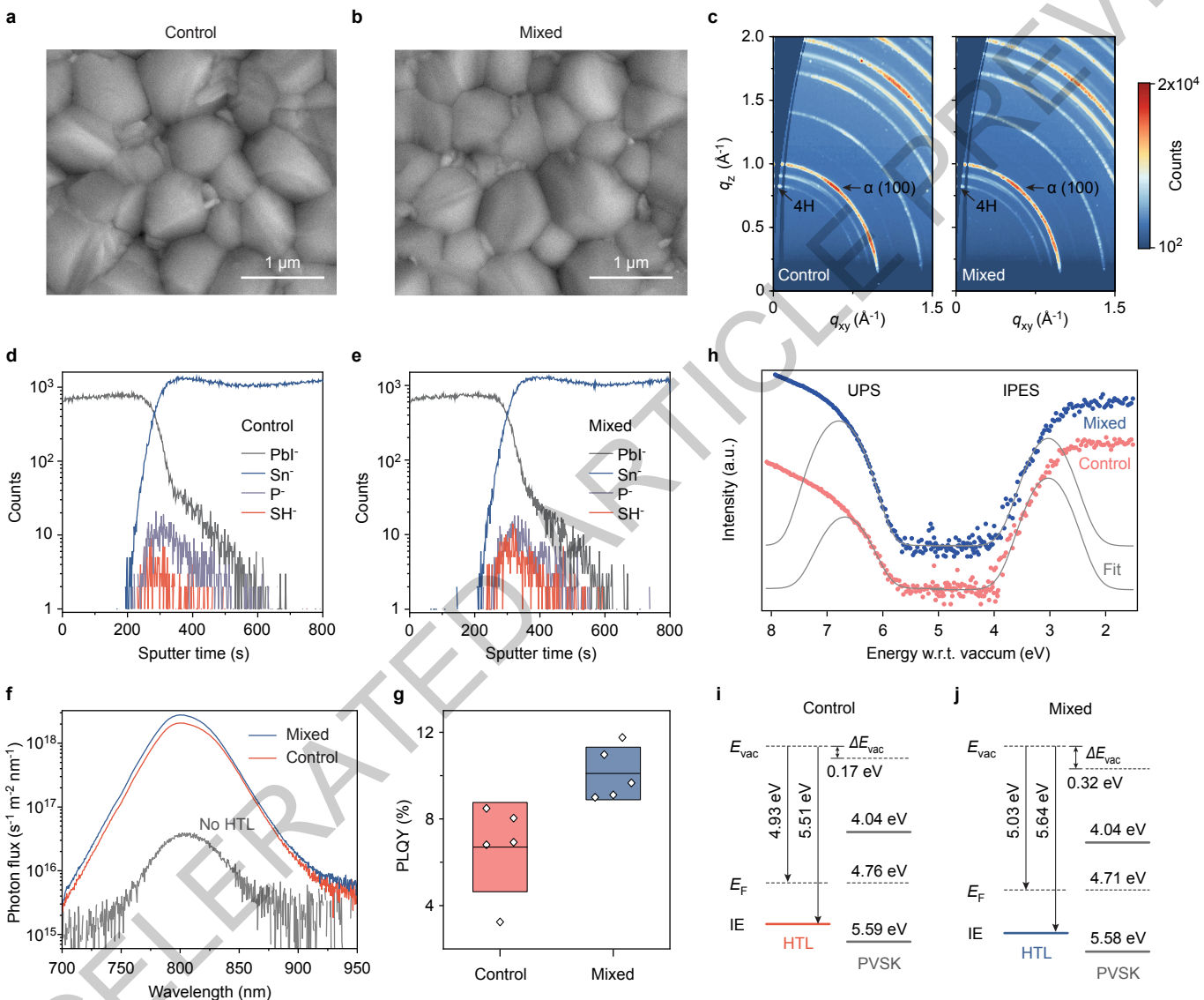
2PACz

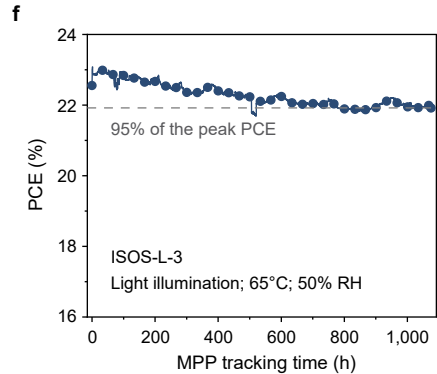
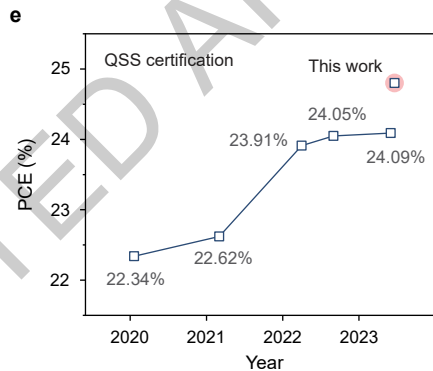
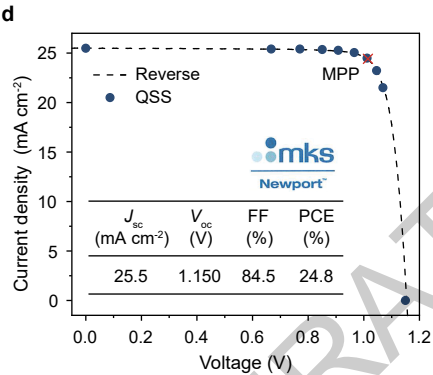
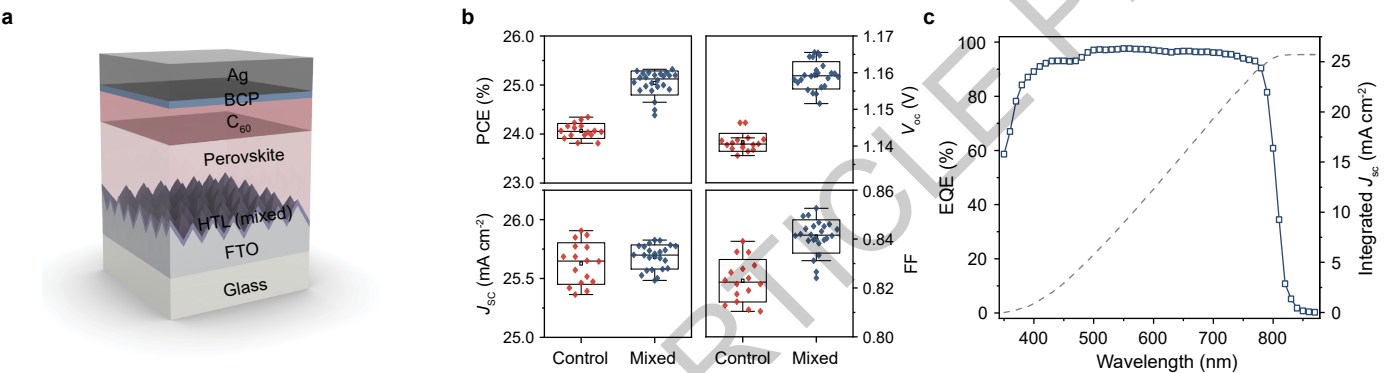


3-MPA

**d****e****b****c****f**









## Solar Cells Reporting Summary

Nature Research wishes to improve the reproducibility of the work that we publish. This form is intended for publication with all accepted papers reporting the characterization of photovoltaic devices and provides structure for consistency and transparency in reporting. Some list items might not apply to an individual manuscript, but all fields must be completed for clarity.

For further information on Nature Research policies, including our [data availability policy](#), see [Authors & Referees](#).

## ▶ Experimental design

## Please check: are the following details reported in the manuscript?

## 1. Dimensions

- Area of the tested solar cells  Yes 0.049 cm<sup>2</sup>  
 No
- Method used to determine the device area  Yes The active area was determined by the aperture shade mask (0.049 cm<sup>2</sup>) placed in front of the solar cell  
 No

## 2. Current-voltage characterization

- Current density-voltage (J-V) plots in both forward and backward direction  Yes Figure 4d (reverse and quasi-steady-state scans)  
 No
- Voltage scan conditions  Yes Supplementary Figure 21  
*For instance: scan direction, speed, dwell times*  
 No
- Test environment  Yes Supplementary Figure 21  
*For instance: characterization temperature, in air or in glove box*  
 No
- Protocol for preconditioning of the device before its characterization  Yes No preconditioning is needed  
 No
- Stability of the J-V characteristic  Yes Supplementary Fig. 20b  
*Verified with time evolution of the maximum power point or with the photocurrent at maximum power point; see ref. 7 for details.*  
 No

## 3. Hysteresis or any other unusual behaviour

- Description of the unusual behaviour observed during the characterization  Yes PCE from reverse scan matches well with those from the quasi-steady-state scan and steady-state measurements.  
 No
- Related experimental data  Yes Figure 4d and Supplementary Fig. 20  
 No

## 4. Efficiency

- External quantum efficiency (EQE) or incident photons to current efficiency (IPCE)  Yes Figure 4c  
 No
- A comparison between the integrated response under the standard reference spectrum and the response measure under the simulator  Yes The difference was found to be less than 1.5% (Main text - Solar cell efficiency and stability)  
 No
- For tandem solar cells, the bias illumination and bias voltage used for each subcell  Yes Not relevant  
 No

## 5. Calibration

- Light source and reference cell or sensor used for the characterization  Yes Methods - Solar cell characterization  
 No
- Confirmation that the reference cell was calibrated and certified  Yes Methods - Solar cell characterization  
 No



- Calculation of spectral mismatch between the reference cell and the devices under test  Yes  No M = 1.019 for the certified device
6. Mask/aperture
- Size of the mask/aperture used during testing  Yes  No 0.049 cm<sup>2</sup>
- Variation of the measured short-circuit current density with the mask/aperture area  Yes  No The accuracy of short-circuit current density was confirmed from EQE measurements.
7. Performance certification
- Identity of the independent certification laboratory that confirmed the photovoltaic performance  Yes  No Newport
- A copy of any certificate(s)  
*Provide in Supplementary Information*  Yes  No Supplementary Figure 21
8. Statistics
- Number of solar cells tested  Yes  No Figure 4b and Supplementary Figure 22
- Statistical analysis of the device performance  Yes  No Figure 4b and Supplementary Figure 22
9. Long-term stability analysis
- Type of analysis, bias conditions and environmental conditions  
*For instance: illumination type, temperature, atmosphere humidity, encapsulation method, preconditioning temperature*  Yes  No Figure 4f, Supplementary Figure 26 and Supplementary Figure 28